Direct observation of defect structure in protein crystals by atomic force and transmission electron microscopy

Genevieve Devaud,* Paul S. Furcinitti,‡ John C. Fleming,* Mary K. Lyon,* and Kenneth Douglas*

Departments of *Physics, and ‡Molecular, Cellular and Developmental Biology, University of Colorado, Boulder, Colorado 80309 USA

ABSTRACT We have examined the structure of S-layers isolated from *Sulfolobus acidocaldarius* using atomic force microscopy (AFM) and transmission electron microscopy (TEM). From the AFM images, we were able to directly observe individual dimers of the crystal, defects in the crystal structure, and twin boundaries. We have identified two types of boundaries, one defined by a mirror plane and the other by a glide plane. This work shows that twin boundaries are highly structured regions that are directly related to the organization of units within each crystal domain. Projection maps from TEM images have shown that there are significant differences in the final average maps, depending on which side of the sample is adsorbed to the carbon support film. Comparison of AFM images to TEM projection maps has allowed us to relate high magnification views obtained by AFM to the relatively high resolution information obtained by electron microscopy and image processing.

INTRODUCTION

The atomic force microscope (AFM) has opened doors to the study of atomic structure and surface morphology of both inorganic and organic materials (Hansma et al., 1988). In particular, structures of biological materials can now be directly imaged by AFM and compared with filtered images, or calculated projection maps, obtained from transmission electron microscopy (TEM) images. Thus, AFM offers a unique complement to TEM, as it allows the direct observation of surface structure at high magnification.

We have reinvestigated the structure of the S-layer of *Sulfolobus acidocaldarius* using AFM, as well as TEM. S-layers are the outermost layers of certain bacteria and consist of glycoproteins arranged in a two-dimensional crystalline array (for review, see Sleytr, 1978). The structure of *S. acidocaldarius* was originally determined by electron microscopy and image processing (Taylor et al., 1982). The structure consists of dimers arranged into triads, with triads surrounding a large central pore. Though the symmetry of the structure has since been determined to be P3 (Lembcke et al., 1990) rather than P6, the essential findings of the earlier work remain correct. In this paper, we contrast and compare results obtained by AFM of metallized S-layers and TEM of negatively stained S-layers.

EXPERIMENTAL METHODS

Sulfolobus acidocaldarius was obtained from American Type Culture Collection (Rockville, MD) and grown at 70°C in a liquid medium, modified from the original formula of Brock et al. (1972): 9.1 μM $MnCl_2 \cdot 4H_2O$, 12 μM $Na_2B_4O_7 \cdot 10 H_2O$, 7.7 μM $ZnSO_4 \cdot 7H_2O$, 0.37 μM $CuCl_2 \cdot H_2O$, 0.35 μM $NaNO_3$, 0.065 μM $CoSO_4 \cdot H_2O$, 9.8 mM $(NH_4)_2SO_4$, 2.1 mM KH_2PO_4, 2.1 mM $MgSO_4$, 0.48 mM

$CaCl_2 \cdot 2H_2O$, 74 μM $FeCl_3 \cdot 6H_2O$ (all from Sigma Chemical Co., St. Louis, MO), and 1.0 g Yeast Extract (BBL, Cockeysville, MD).

S-layers were isolated from 3 liters of log phase cells, using a modification of the procedure of Michel et al. (1980). Cultures were brought to pH 7.0 with $NaHCO_3$ and cells collected by centrifugation for 20 min at 10,000 g. Pellets were resuspended in 150 ml of 2 mM EDTA (disodium salt), 10 mM Hepes pH 5.0 (Sigma Chemical Co.), and stirred for 5 min before adding 150 mg SDS (Bio-Rad, Richmond, CA). After 5 min, $MgCl_2$ was added to 5 mM, followed by the addition of a small amount of DNase I (Sigma Chemical Co.). After 15 min, 50 ml of 8% SDS was added and the sample was stirred for 48 h, followed by centrifugation at 56,000 g for 20 min. The sample was resuspended in 2% SDS and left stirring for 1 h at 60°C. At this point, the preparation consisted of whole sacs of S-layers, with some debris. To remove debris and SDS, the sacs were repeatedly centrifuged (56,000 g for 20 min) and resuspended in distilled water. Generally five to eight washes were done, and the final pellets were resuspended in ~3 ml distilled water and stored at 4°C.

To obtain sheets, 1-ml aliquots were sonicated, using a Branson Sonifier 250 (Branson Ultrasonics Corp., Danbury, CT), with a duty cycle of 50% and output control of 1. Four cycles of 20 s sonication, 10 s rest were done. Differential centrifugation was used to separate sacs and various size sheets, with the series consisting of 12,000 g for 15 min, 12,000 g for 30 min, 12,000 g for 30 min, and 48,000 g for 30 min. The two 12,000 g × 30-min runs consistently yielded clean, monolayer fragments.

Atomic force microscopy

S-layers were deposited onto freshly cleaved highly ordered pyrolytic graphite (HOPG, ZYA grade; Union Carbide Corp., Cleveland, OH), then were metallized for AFM assay. Titanium metal was deposited by electron beam evaporation at an angle of 50 degrees from normal in an Edwards E306A (Edwards High Vacuum International, Wilmington, MA) vacuum deposition system. After deposition and a cooling period for the gun, the chamber was returned to atmospheric pressure with dry nitrogen and the samples removed. An average thickness of 1.2 nm of titanium metal was measured in vacuo during deposition with an IC6000 quartz crystal monitor (Edwards High Vacuum International). An independent measurement of the metal thickness was done by spectroscopic ellipsometry of a representative oxidized titanium film deposited onto bare quartz. That thickness was found to be 3.5 nm.

Atomic force microscopy was done with a Digital Instruments Nanoscope II (Goleta, CA). Commercial tips with a variety of force constants were obtained from Digital Instruments and Park Scientific (Sunny-

---

vale, CA). The value of the force constant did not appear to affect the quality of the images obtained. The AFM was operated at zero net force with a typical scan speed of 8.68 or 19.53 Hz, an integral gain of 5.0, a proportional gain of 7.0, and a two-dimensional gain of 0.0. All imaging was done in air at room temperature.

Filtered images were obtained using Nanoscope II software supplied by Digital Instruments. The two-dimensional FFT of the raw image was displayed, rectangular passband were drawn, and the inverse transform was performed to obtain the filtered image.

Electron microscopy

S-layers (in either distilled water or 2.5 mM Hepes, pH 7.0, 50 mM NaCl) were applied to a carbon film on 400 mesh copper grids and strained with 2% uranyl acetate in distilled water (Polysciences, Warrington, PA). The Hepes-NaCl solution aided in adsorbing the extracytoplasmic side to the substrate. No difference in the samples was observed other than the relative proportions of sides adsorbed to the substrate. Micrographs were taken on a Philips CM 10 (Philips Electronic Instruments, Mahwah, NJ), using low dose techniques and Kodak SO163 film (Kodak Park, Rochester, NY), with a voltage of 100 kV, 70 μm objective aperture, defocus of $\sim$50 nm, and magnification of 41,040.

Image processing

Cytoplasmic and extracytoplasmic views from the same negative were digitized with a Photometrics STAR I, cooled-CCD camera operating at $-45°C$ (Photometrics, Ltd., Tucson, AZ). The camera system was interfaced with a Digital Equipment Corporation (DEC, Maynard, MA) VAXStation 3200 through a National Instruments GPIB board (Austin, TX). Image acquisition software was written at the University of Colorado in VMS FORTRAN. This program makes use of a National Instruments GPIB software driver and Photometrics internal camera commands. The camera system included a Micro-Nikkor lens ($f = 55$ mm, 1:2.8) (Nikon Inc., Torrance, CA), a 550-nm interference band pass filter (to reduce glare from long wavelength light) (Melles Griot, Irvine, CA), and a 0.9 ND filter (to reduce the light intensity) (Tiffen Manufacturing Corp., Hauppauge, NY). The camera software allows corrections to be made for dark current, uneven illumination, and variable sensitivity of the cells in the CCD chip. The final pixel size was 0.56 × 0.56 nm and transmitted light intensity was converted computationally to optical density.

The SPIDER software system (Frank et al., 1981) was used for image processing. A suitable area was selected interactively on a Parallax 1280-Q-24VN image display system (Parallax Graphics, Santa Clara, CA). In order to calculate an initial reference image, the Fourier Transform (FT) and power spectrum were calculated and the diffraction pattern indexed. The indexing was used to calculate a Fourier filter mask that was applied to the FT to produce a filtered image. A subarea of the filtered image was used as a reference in cross-correlation mapping of similar areas in the raw image. Areas centered on the peaks in the cross-correlation map were extracted from the raw images and averaged. This is the correlation averaging method developed by several groups (Saxton, 1980; Frank and Goldfarb, 1980; Saxton and Baumeister, 1982). Averages from several areas of the negatives were calculated in a similar fashion. The average with the best power spectrum was chosen as the new reference and all the other images were aligned to it (translationally by cross-correlation and rotationally by angular cross-correlation of the auto-correlation functions). The aligned images were then submitted to correspondence analysis (Bretaudiere and Frank, 1986) to select similar particles for averaging.

The cytoplasmic and extracytoplasmic average images were subtracted to give a difference map. The pixel-to-pixel variance image was also calculated for the cytoplasmic and extracytoplasmic sides and used to calculate a standard error of the mean for each pixel in the difference map. Differences greater than or less than three standard errors of the mean above or below zero were retained (Furcinitti et al., 1989).

The resolution of the AFM images was estimated to be slightly better than 10 nm, calculated from the highest order reflection of the power spectrum displayed on a Nanoscope II monitor.

RESULTS

The atomic force microscope can be used to directly image surfaces at very high magnification as a complement to the relatively high resolution obtainable by TEM. Fig. 1 A shows a high magnification AFM image of the cytoplasmic surface of the S-layer of S. acidocaldarius. Light areas represent regions where the sample was retracted from the tip (high elevation areas of the sample) and dark areas represent areas where the sample was extended towards the tip (low elevation areas of the sample). Each white triangle consists of a triad of S-layer protein and the triads are organized such that a hexagonal array of large cytoplasmic pores is evident. More difficult to see are the two distinct arrays of small pores, one set marked A, the other B. The triads are generally rotated $\sim$10 degrees with respect to the line connecting their centers, a rotation that was also observed in TEM images. This image shows P3 symmetry.

Additionally, because the AFM images the structure of the surface only, sidedness of the S-layer is easily distinguished. A fragment of a broken sacculus of S. acidocaldarius is shown in Fig. 1 B. The lower portion of the sac is the cytoplasmic surface (C). The upper portion (top portion of the fold) is extracytoplasmic (E). The extracytoplasmic surface does not show the clearly defined large pore structure that is characteristic of the cytoplasmic surface. In fact, we observed that the substructure of the E-surface was much less well defined, even on fragments of S-layer that were directly adsorbed to the substrate. This may be due to the carbohydrate chains which are associated with the S-layer proteins on the extracytoplasmic surface (Michel et al., 1980).

Two types of extraneous material on the S-layer surface are shown in Figs. 1 B and 2. In one case, the material is adsorbed onto the surface of the S-layer (Fig. 1 B, arrow) and is probably due to contamination produced during sample preparation. In the second case, the material appears to be in the plane of the S-layer (Fig. 2, short arrow), and disrupts the hexagonal pattern of large cytoplasmic pores. The latter type of inserted material can be considered to be a point defect in the crystal structure.

Twin boundaries were found in some of the S-layer sheets (Fig. 2). The location of the twin boundary can be readily discerned by observing a change in orientation of the triads from the upper to lower portion of Fig. 2. The arrangement of individual triads is more easily observed in a filtered image of this area (Fig. 3 A). There are two types of boundaries illustrated in Fig. 3 B. Boundary A is characterized by rows of "dogbones", two triads that share the central dimer. Boundary A acts as a mirror plane, where triads are reflected across the boundary. Boundary B is characterized by sharing of two dimers
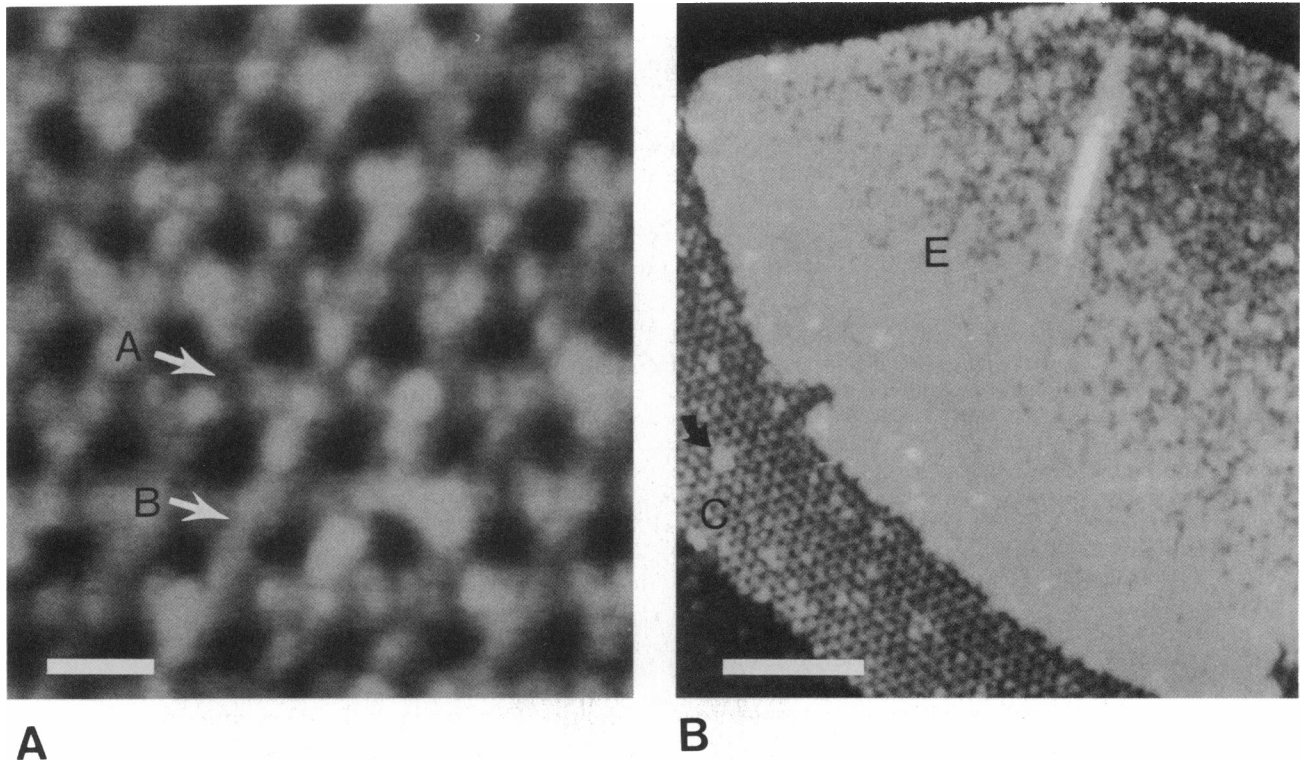
FIGURE 1 (*A*) AFM image of Ti-coated S-layer, showing the basic structure of triads surrounding large pores. The two types of smaller holes in the structure are indicated by the arrows, marked *A* and *B*. The small hole (*B*) found within the pore is almost completely obscured by the metal-coating. Bar = 25 nm. (*B*) AFM image showing a partially opened sac of S-layer. The extracytoplasmic side (*E*) does not show the lattice nearly as clearly as the cytoplasmic side (*C*). The arrow points to additional material on the surface of the S-layer. Bar = 250 nm.

per triad. In this case, the boundary acts as a glide plane; triads are reflected across the boundary and translated. Interestingly, the pattern of large cytoplasmic holes is not disrupted at the twin boundary (Figs. 2 and 3 *A*).

The distinction between cytoplasmic and extracytoplasmic surfaces is equally distinct with negatively stained samples in the electron microscope (Fig. 4, *A* and *B*). The two images shown were on the same negative, ensuring similarity of stain and defocus levels. The predominant features of the cytoplasmic surface are large, stain-filled holes (*arrow,* Fig. 4 *B*), surrounded by roughly triangular-shaped units, each of which has a small, central hole. The extracytoplasmic surface (Fig. 4 *A*) has small three-lobed holes (*arrow*). The large hole seen on the cytoplasmic side is almost completely obscured on the extracytoplasmic side (*arrowhead,* Fig. 4 *A*). The large hole contains stain-excluding "arms" that form a basket structure (Taylor et al., 1982), thus making it very difficult to see on the extracytoplasmic side. Point defects and twin boundaries were sometimes visible, but these defects were visible only on the cytoplasmic surface. The insets in Fig. 4 are the power spectra of two sides of the S-layer, respectively; they can be used to estimate the resolution of the data from the highest order spots in the pattern. For the cytoplasmic side this corresponds to a resolution of 2.1 nm and for the extracytoplasmic side the resolution is 2.6 nm. Preliminary refer-

ence images for image processing were obtained by indexing these power spectra and using standard lattice filtering techniques.

The respective references were cross-correlated with the images from the extracytoplasmic and cytoplasmic sides of the S-layer. The cross-correlation peak maps are shown in Fig. 5, *A* and *B*. Areas around each peak were extracted from the images and averaged. The new average was employed to refine the angular and translational alignments of the extracted subareas. Correspondence analysis was used to identify similar images to participate in the final averages. The resolution of the averages was determined by examining their power spectra and using the highest order spots. This method gave resolution limits of 2.35 nm for both the extracytoplasmic and cytoplasmic averages. The resolution was also estimated using the spectral signal-to-noise ratio (Unser et al., 1987) and the resolution was 2.4 and 2.58 nm for the extracytoplasmic and cytoplasmic averages, respectively. The average images were low pass filtered to 2.4 nm.

Fig. 5, *C* and *D* show the final averages for the extracytoplasmic and cytoplasmic sides. The mirror image of the extracytoplasmic average was rotated and translated to coincide with the cytoplasmic average. Significant positive and negative differences between the averages of the two sides are shown in Fig. 5, *E* and *F*. There is extra
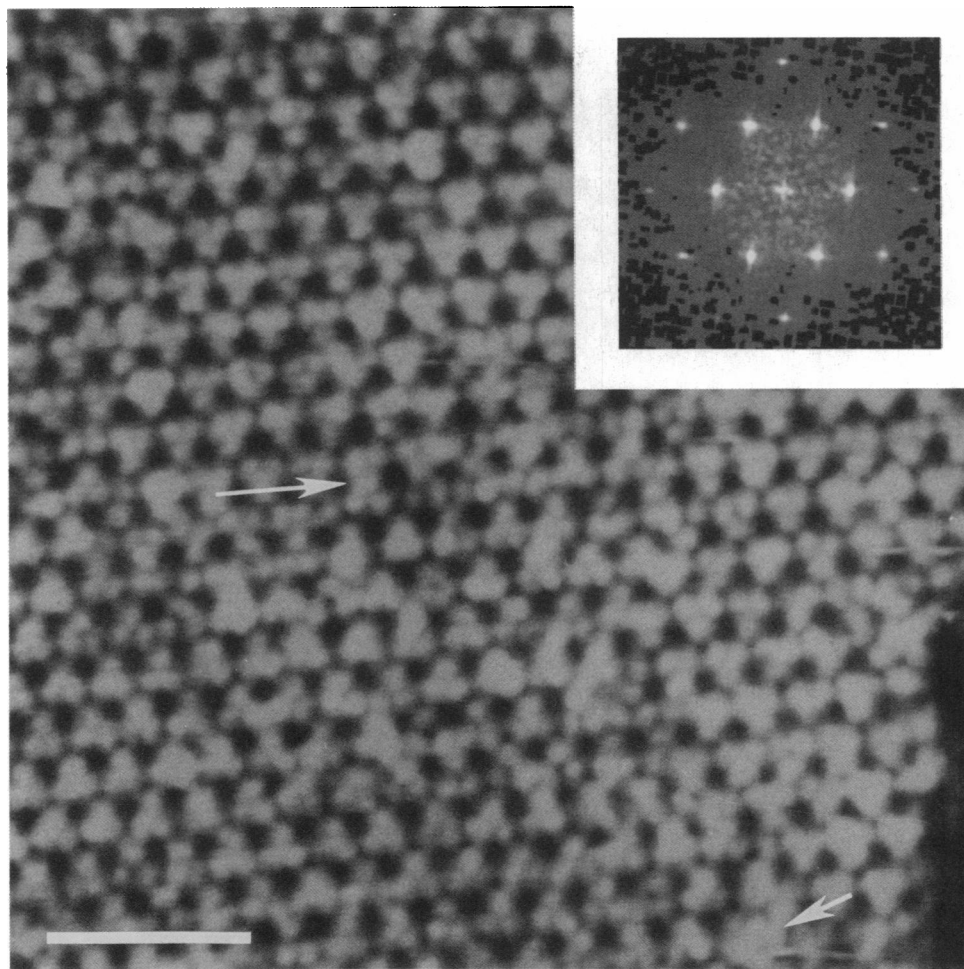
FIGURE 2 AFM image that shows numerous types of defects, including extra material (*short arrow*), shared dimers (*long arrow*), and a twin boundary. The twin boundary can be most clearly seen in the filtered version of this image, Fig. 3 *A*. (*Inset*) FT of Fig. 2. Bar = 100 nm.

density in the "baskets" in the sixfold related large cavities in the extracytoplasmic sides (Fig. 5 *E*) and also extra density in the threefold cavities between the protein triads in the cytoplasmic side (Fig. 5 *F*). Differences in the cavities in the center of the protein triads are not statistically significant.

For comparison of AFM and TEM images, the projection map of the cytoplasmic side was filtered at a resolution of 10 nm and compared with an extremely high magnification view obtained by AFM (Fig. 6, *A* and *B*). There is good agreement between the two images, with one exception. The trilobed hole found within each triad is almost invisible in the AFM images, though both trilobed holes are obvious in the TEM images.

The area of a twin boundary was examined in a TEM image (Fig. 6 *C*). Twin boundaries can be located by observing the change in orientation of the triads, as shown. However, the structure at the boundary is extremely ambiguous in TEM images when viewed at high magnification, unlike high magnification AFM images. Therefore, "dogbones" could not be clearly observed, even when a twin boundary was located, though the sug-

gestion of a shared dimer is seen at the exact boundary between two rows (*arrow,* Fig. 6 *C*). This would appear to be a "dogbone" of the type shown in Fig. 3 *C* (3). The rotation of the triads relative to the line connecting their centers is also apparent in Fig. 6 *C*. Comparing the lower left area of Fig. 6 *C* with Fig. 1 *A* provides a clear contrast between an AFM image and a TEM image of cytoplasmic sides with similar orientations.

DISCUSSION

Types of defects visible

Images of S-layers obtained with the AFM revealed distinct types of defects: point defects (inserts) and line defects (twin boundaries composed of rows of shared dimers or "dogbones"). Inserts were of two types: material inserted into the various holes but not extending over or under the planes of the S-layer, and material both in the holes and on the surfaces of the S-layers. Shared dimers ("dogbones") were commonly associated with the boundaries of twinned crystal domains (Figs. 2 and
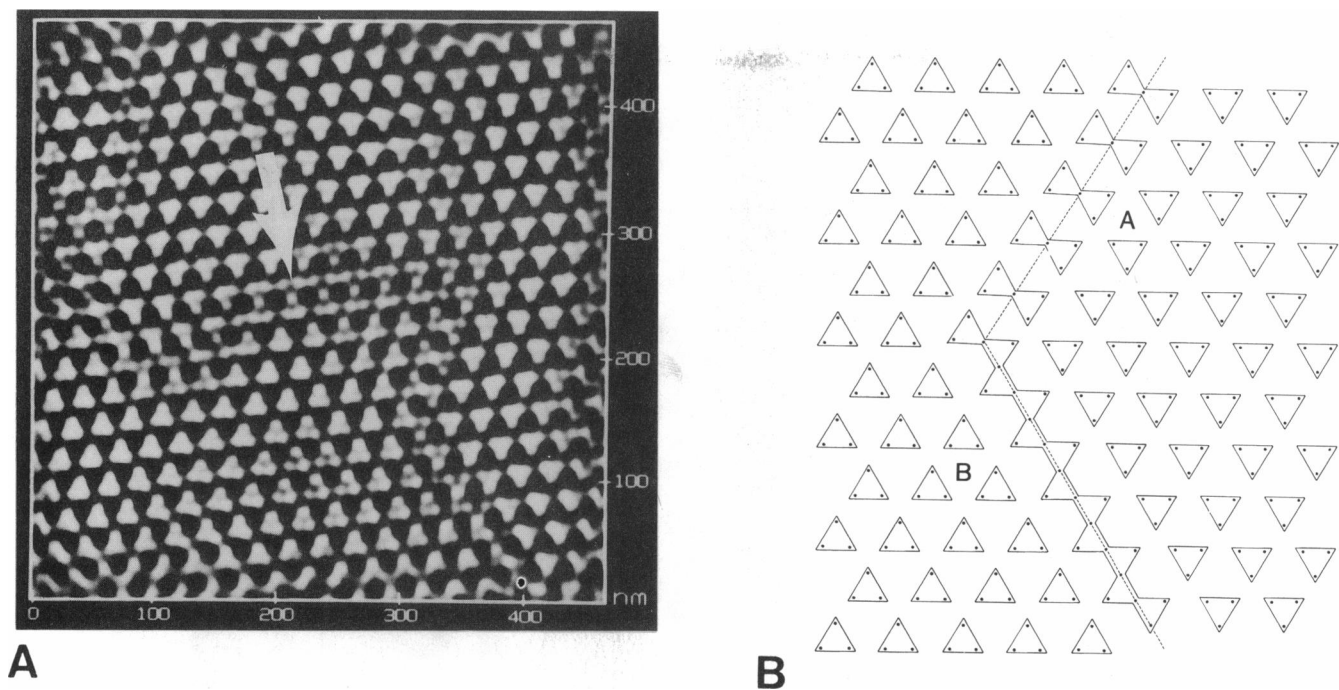
FIGURE 3 (*A*) Filtered topview image of the AFM image shown in Fig. 2. The location of the twin boundary can be readily discerned by observing a change in orientation of the triads. The twin boundary is composed of rows of shared dimers, or "dogbones" (*arrow*). (*B*) Diagram of the two types of arrangements found at twin boundaries. Boundary *A* has a mirror plane and is characterized by the "dogbone" shapes. Boundary *B* has a glide plane and is characterized by two shared dimers per triad.

3). It should be noted that bent or stretched lattices were also observed on occasion, but in most cases these were probably distortions caused during drying of the S-layer onto the substrate. Distortion during drying also might account for the variation in the alignment of the triad bases within an individual row.
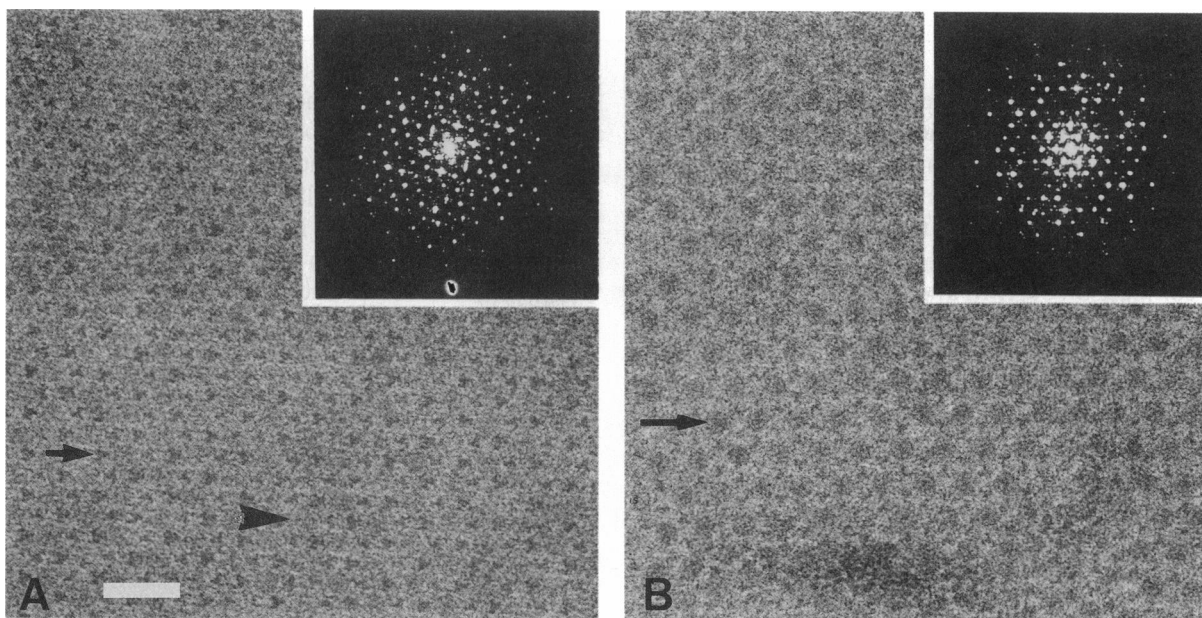

FIGURE 4 (*A*) TEM image of negatively stained S-layer, with the extracytoplasmic side up. The predominant features are trilobed, stain-filled areas (*arrow*). The large hole seen on the cytoplasmic side is almost completely obscured on the extracytoplasmic side (*arrowhead*). (*B*) TEM image of S-layer with the cytoplasmic side up. Here, the large pore is almost completely filled with stain (*arrow*). Insets are of the power spectra of each image. Bar = 40 nm.
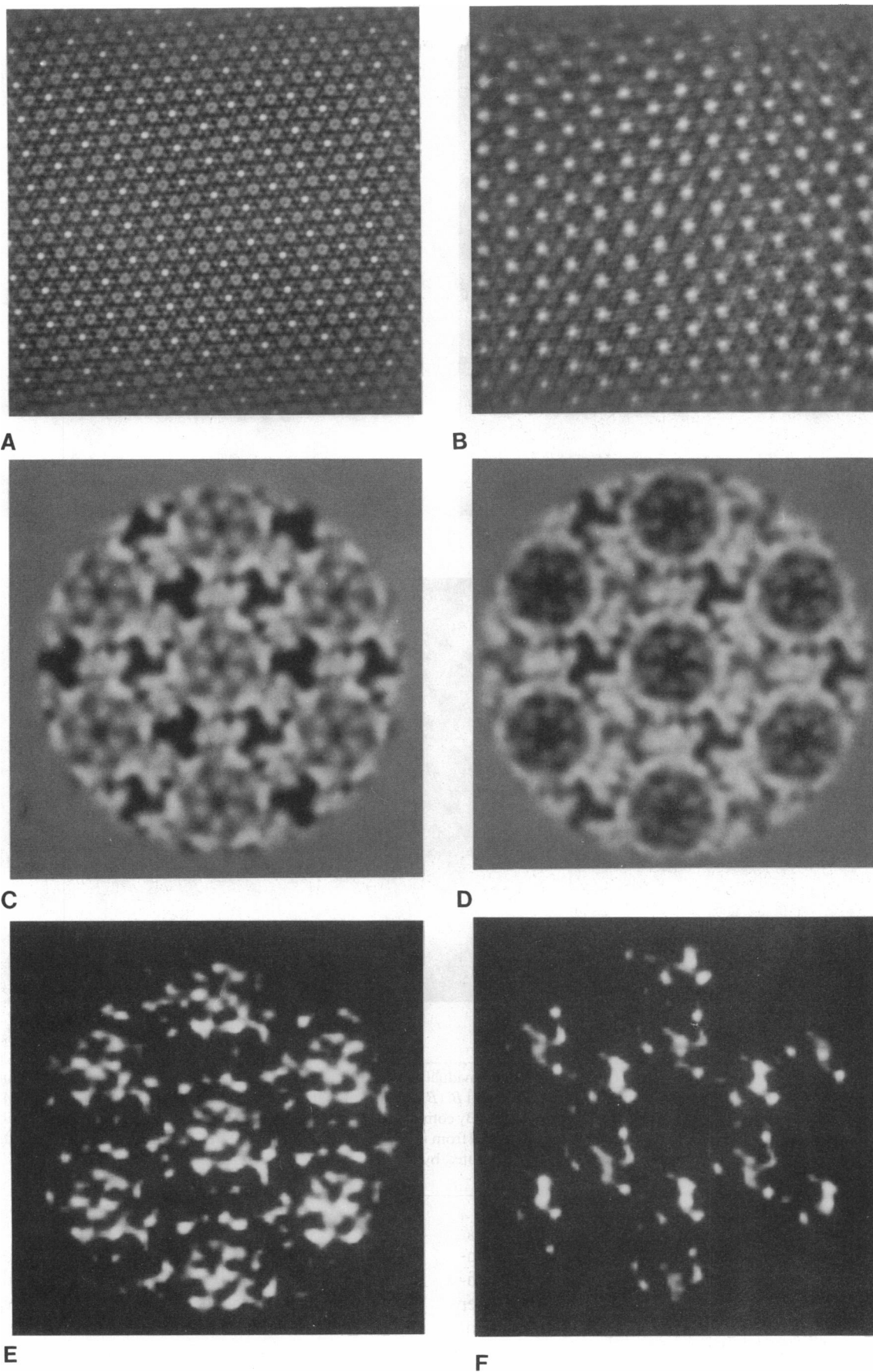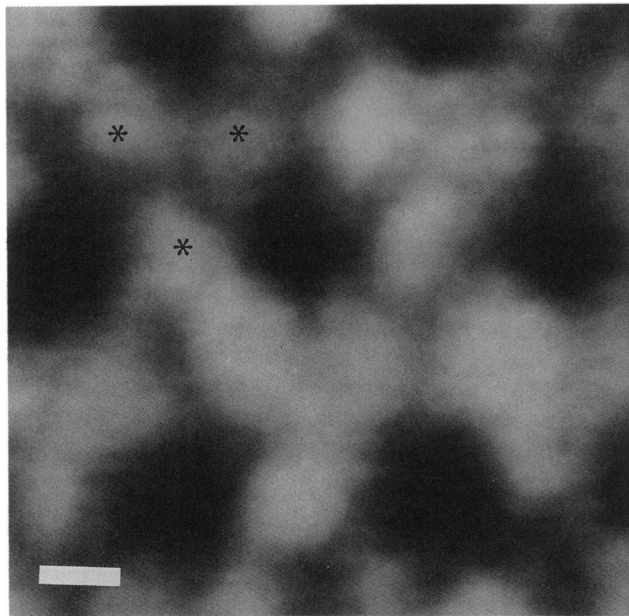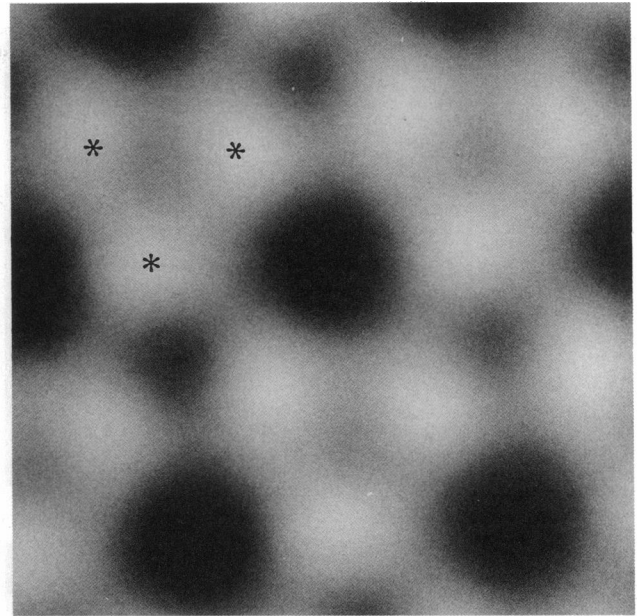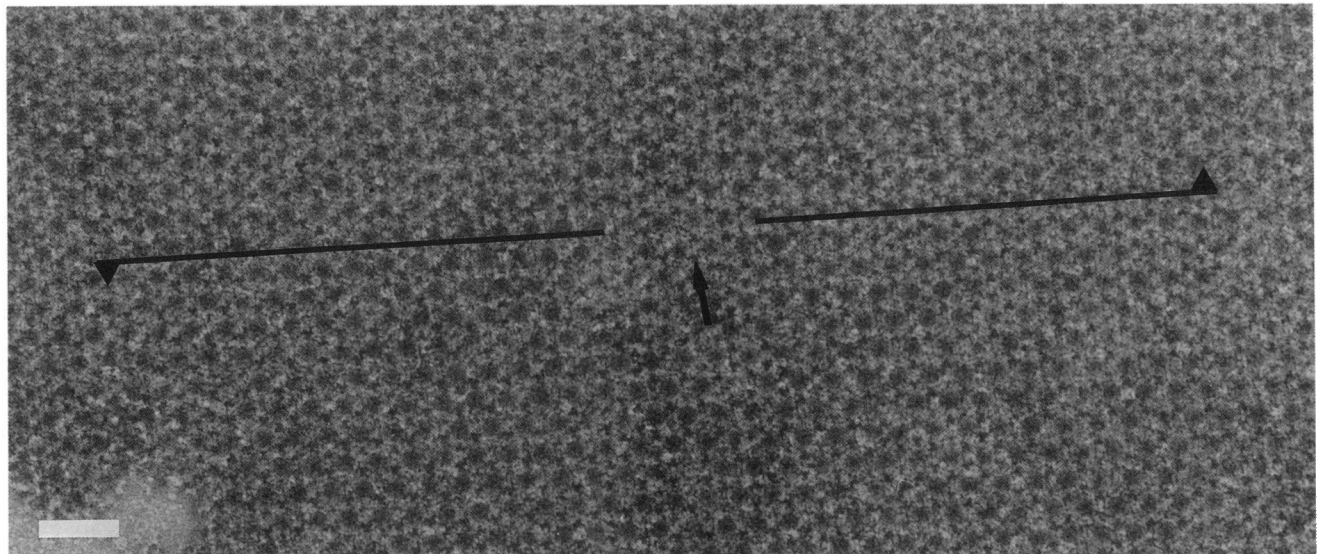
FIGURE 5 (*A* and *B*) Cross-correlation functions of the reference images with the extracytoplasmic and cytoplasmic sides, respectively. (*C* and *D*) Final averaged images, again of the extracytoplasmic and cytoplasmic sides. Differences in the projection maps are readily apparent. (*E* and *F*) Negative and positive difference maps between *C* and *D*.

FIGURE 6 (A) AFM image at a magnification of 1,850,000. The individual dimers which make up a triad can be clearly seen. Three dimers of one triad are marked with asterisks in the upper left corners of both A and B. (B) Projection map of the cytoplasmic side, derived from TEM image and filtered to 10 nm resolution for direct comparison with AFM image. By comparing the projection maps with the AFM images, it is possible to relate the higher resolution data obtained from TEM to the images obtained from the AFM. Bar = 18.5 nm. (C) TEM image of cytoplasmic side in an area that includes a twin boundary. The direction of each triad is indicated by triangles along one row. At the twin boundary, an arrow indicates a possible "dogbone" shape. Bar = 660 nm.

Certain deviations from perfect crystallinity are undoubtedly native to the crystals. For example, it is difficult to imagine how twinning or the sharing of a dimer could be induced during sample or grid preparation. Point defects either could be native or created during sample preparation. Debris might well be inserted in the holes of the S-layer during sonication or during grid preparation.

Implications and consequences

The observation of naturally occurring defects and multiple crystal domains suggests several possibilities regarding their function. First, it is clear that S. acidocaldarius can tolerate errors in the lattice structure of the S-layer. However, it should be noted that the rows of large cytoplasmic holes remain ordered at the twin boundaries. Even in this defect area, each large cytoplasmic pore is

surrounded by six dimers. Fingers extend from each of the dimers, so that even if the "dogbone" arrangement is deviant, it is quite likely that the "baskets" in the pores (Taylor et al., 1982) are essentially intact. Missing baskets were never observed in TEM images of the extracytoplasmic sides. Thus, there does not appear to be a row of defective pores with empty holes that could create a weak point in the S-layer at the twin boundaries. Second, it seems likely that the defects and the existence of multiple domains are related to the fact that these are lobed bacteria with irregular surfaces (Brock, 1972). A surface that encases a lobed shaped object is likely to require line defects. The shared dimers were found at twin boundaries, areas that may need the most flexibility to form a lobe. The deviations from perfect order of the triads found in the vicinity of twin boundaries are systematic variations in the crystal structure. These variations would form the boundaries between two crystal domains without a physical break in the S-layer while minimizing the disruption to the overall pattern, particularly the cytoplasmic holes.

Structural studies: AFM as a complement to TEM

Detailed structural information regarding two-dimensional crystals is now routinely obtained by means of low dose electron microscopy, followed by analysis of the diffraction patterns and reconstruction of the structure (for an early review of theory and techniques, see Amos et al., 1982). Defects in the structure degrade the resolution obtainable in the final reconstruction. Twinned crystals can actually be sufficiently misleading to result in the determination of an incorrect structure. It is now possible to examine the surfaces of two-dimensional crystals in great detail, using atomic force microscopy. With AFM one can determine the relative cleanliness of a preparation, and the approximate density and types of defects present. Point defects are very difficult to see by electron microscopy and are generally inferred to be part of the problem when a two-dimensional crystal has particularly poor resolution. Twinning can be determined by correlation averaging of individual images (Lembcke et al., 1990), but is not directly observable by electron microscopy. Thus, it would seem to be highly advantageous to examine two-dimensional crystals by AFM as well as by electron microscopy and image processing.

The resolution of the images obtained by AFM was relatively low (10 nm). On the other hand, very high magnification, high contrast images that could readily be interpreted were obtained. Only the AFM images gave information on how individual dimers fit together at the twin boundary. Equally high magnification pictures cannot be obtained by TEM without using high doses of electrons. Thus, the two imaging techniques complement each other in terms of the information they can provide. AFM provides a characterization of the surface

and of the arrangement of individual dimers, whereas TEM provides high resolution data on averaged dimers. High resolution information obtained from TEM can eventually be used to model the positioning and interactions of individual dimers, even at noncrystalline areas such as twin boundaries that have been directly observed by AFM.

A second issue is the difference in appearance of the two sides of a single layer crystal and the effect this has on the final reconstruction. It is clear that in the particular case of S. acidocaldarius the S-layers have two very distinct sides, regardless of whether they are imaged by AFM or TEM. Defects, particularly twinning, are obvious on the cytoplasmic side. One would expect to see differences between the two sides with AFM, as this is an imaging method that looks at surfaces. However, it is somewhat surprising that the two sides are so distinct with negatively stained samples in the TEM, where the imaging method is to look through the sample. This phenomenon has been observed before with S-layers (Michel et al., 1980; Lembcke et al., 1990). However, the fact that the differences in the two sides result in different projection maps had not been clearly shown. The possible reasons for this difference in the final maps include: flattening of the protein on the side against the grid, stain penetration differences dependent on which side is up, differences in the degree to which the entire structure collapses with drying, and actual differences in the structure of the protein on the two sides. The most obvious way to avoid the artifactual problems is to record electron microscope images only of frozen, hydrated samples over holes (for example, Milligan et al., 1990). This is not always possible, so it would be best to analyze negative stain images of each side separately and examine projection maps of each, in order to determine if there are significant differences between them. Again, AFM images of each side may help in evaluating the significance of any differences in the projection maps.

CONCLUSIONS

The atomic force microscope has proven to be a powerful tool for imaging surface topography of two-dimensional protein crystals. It clearly allows one to see individual dimers and twin boundaries, features that are not easily visible in TEM. Thus, it will undoubtedly prove to be a valuable tool when used in conjunction with electron microscopy and image processing.

The most important finding of this work is that twin boundaries in two-dimensional crystals are highly structured areas. At boundaries, two S-layer crystal domains merge in such a way as to preserve the overall pattern of pores. The boundaries themselves can be defined crystallographically, consisting of either a glide plane or mirror plane, depending on the orientation of the domains at their junction. It is likely that twin boundaries in other two-dimensional crystals are equally structured.

REFERENCES

Amos, L., R. Henderson, and P. N. T. Unwin. 1982. Three-dimensional structure determination by electron microscopy of two-dimensional crystals. *Prog. Biophys. Mol. Biol.* 39:183–231.

Bretaudiere, J. P., and J. Frank. 1986. Reconstitution of molecule images analyzed by correspondence analysis: A tool for structural interpretation. *J. Microscopy.* 144:1–14.

Brock, T. D., K. M. Brock, R. T. Belly, and R. L. Weiss. 1972. *Sulfolobus:* A new genus of sulphur-oxidizing bacteria living at low pH and high temperatures. *Arch. Microbiol.* 84:54–68.

Frank, J., and W. Goldfarb. 1980. Methods for averaging of single molecules and lattice-fragments. *In* Electron Microscopy at Molecular Dimensions. W. Baumeister and W. Vogell, editors. Springer-Verlag, Heidelberg. 261–269.

Frank, J., B. Shimkin, and H. Dowse. 1981. SPIDER: A modular software system for electron image processing. *Ultramicroscopy.* 6:343–358.

Furcinitti, P. S., J. van Oostrum, and R. M. Burnett. 1989. Adenovirus polypeptide IX revealed as capsid cement by difference images from electron microscopy and crystallography. *EMBO (Eur. Mol. Biol. Organ.) J.* 8:3563–3570.

Hansma, P. K., V. B. Elings, O. Marti, and C. E. Bracher. 1988. Scanning tunneling microscopy and atomic force microscopy: application to biology and technology. *Science (Wash. DC).* 242:209–216.

Lembcke, G., R. Durr, R. Hegerl, and W. Baumeister. 1990. Image analysis and processing of an imperfect two-dimensional crystal: The surface layer of the archaebacterium *Sulfolobus acidocaldarius* re-investigated. *J. Microscopy.* 161(2):263–278.

Michel, H., d.-Ch. Neugebauer, and D. Oesterhelt. 1980. The 2-D crystalline cell wall of *Sulfolobus acidocaldarius:* Structure, solubilization, and reassembly. *In* Electron Microscopy at Molecular Dimensions. W. Baumeister and W. Vogell, editors. Springer-Verlag, Heidelberg. 27–35.

Milligan, R. A., M. Whittaker, and D. Safer. 1990. Molecular structure of F-actin and location surface binding sites. *Nature (Lond.).* 348:217–221.

Saxton, W. O. 1980. Matching and averaging over fragmented lattice. *In* Electron Microscopy at Molecular Dimensions. W. Baumeister and W. Vogell, editors. Springer-Verlag, Heidelberg. 245–255.

Saxton, W. O., and W. Baumeister. 1982. The correlation averaging of a regularly arranged bacterial envelope protein. *J. Microscopy.* 127:127–138.

Sleytr, U. B. 1978. Regular arrays of macromolecules on bacterial cell walls: Structure, chemistry, assembly and function. *Int. Rev. Cytology.* 53:1–64.

Taylor, K. A., J. F. Deatherage, and L. A. Amos. 1982. Structure of the S-layer of *Sulfolobus acidocaldarius. Nature (Lond.).* 299:840–842.

Unser, M., B. L. Trus, and A. C. Steven. 1987. A new resolution criterion based on spectral signal-to-noise ratios. *Ultramicroscopy.* 23:39–52.